

ARTICLE

<https://doi.org/10.1038/s42004-019-0111-x>

OPEN

# Confinement of poly(allylamine) in Preyssler-type polyoxometalate and potassium ion framework for enhanced proton conductivity

Tsukasa Iwano<sup>1</sup>, Satoru Miyazawa<sup>1</sup>, Ryota Osuga<sup>2</sup>, Junko N. Kondo<sup>2</sup>, Kayako Honjo<sup>3</sup>, Takashi Kitao<sup>3,4</sup>, Takashi Uemura<sup>3,4,5</sup> & Sayaka Uchida<sup>1</sup>

Polyoxometalate based solids are promising candidates of proton-conducting solid electrolytes. In this work, a Preyssler-type polyoxometalate is crystallized with potassium ions and poly(allylamine), which is also a good proton conductor, from aqueous solutions. Here we show that the hygroscopicity induced low durability of polyoxometalate and poly(allylamine) can be circumvented by the electrostatic interaction between the polyoxometalate and protonated amine moieties in the solid state. Crystalline compounds are synthesized with poly(allylamine) of different average molecular weights, and all compounds achieve proton conductivities of  $10^{-2} \text{ S cm}^{-1}$  under mild-humidity and low-temperature conditions. Spectroscopic studies reveal that the side-chain mobility of poly(allylamine) and hydrogen-bonding network rearrangement contribute to the proton conduction of compounds with poly(allylamine) of low and high average molecular weights, respectively. While numbers of proton-conducting amorphous polyoxometalate-polymer composites are reported previously, these results show both structure-property relationship and high functionality in crystalline composites.

<sup>1</sup> Department of Basic Science, School of Arts and Sciences, The University of Tokyo, 3-8-1 Komaba, Meguro-ku, Tokyo 153-8902, Japan. <sup>2</sup> Laboratory for Chemistry and Life Science, Institute of Innovative Research, Tokyo Institute of Technology, 4259-R1-10 Nagatsuta, Midori-ku, Yokohama 226-8503, Japan. <sup>3</sup> Department of Applied Chemistry, School of Engineering, The University of Tokyo, 5-1-5 Kashiwanoha, Kashiwa, Chiba 277-8561, Japan. <sup>4</sup> Department of Advanced Materials, Science Graduate School of Frontier Sciences, The University of Tokyo, 5-1-5 Kashiwanoha, Kashiwa, Chiba 277-8561, Japan. <sup>5</sup> CREST, Japan Science and Technology Agency (JST), 4-1-8 Honcho, Kawaguchi, Saitama 332-0012, Japan. Correspondence and requests for materials should be addressed to S.U. (email: [csayaka@mail.ecc.u-tokyo.ac.jp](mailto:csayaka@mail.ecc.u-tokyo.ac.jp))

The performance of cation-conducting solid polymer electrolytes is key to improving the efficiency of fuel cells and secondary batteries. Nafions, which are sulfonated fluorocarbon polymers, have achieved great success commercially in polymer electrolyte fuel cells (PEFCs): Nafions show high proton conductivity ( $>10^{-2} \text{ S cm}^{-1}$ ) under high-humidity (relative humidity (RH) 100%) and low-temperature ( $<373 \text{ K}$ ) conditions<sup>1</sup>. Another example is polyethylene oxides (i.e., high-molecular-weight poly(ethylene glycol)s, PEGs), which can transport cations efficiently ( $10^{-4} \text{ S cm}^{-1}$ ) at room temperature (rt) in next-generation Li- and Na-ion secondary batteries<sup>2–4</sup>. However, these polymers show low durability especially at elevated temperatures, so that composites of polymers with inorganic or carbon-based materials have been fabricated and utilized<sup>5</sup>.

Polyoxometalates (POMs), which are nano-sized anionic metal-oxygen clusters of early transition metals<sup>6–11</sup>, can efficiently transport protons<sup>12–16</sup> since smearing of the negative charge over the external surface oxygens makes the effective surface charge density small. In fact, it has been well known for a long time that Keggin-type acidic POMs (e.g.,  $\text{H}_3[\text{PW}_{12}\text{O}_{40}]$ ,  $\text{H}_4[\text{SiW}_{12}\text{O}_{40}]$ ) show high proton conductivities close to Nafions<sup>17–19</sup>. However, application is limited because the structural stability is low and proton conductivity largely decreases upon slight decrease in RH. To solve these problems, POMs have been hybridized with polymers<sup>20–24</sup> especially with those containing amine groups, which serve as protonation sites. While these POM-polymer composites are promising candidates of future solid electrolytes, it is rather difficult to obtain relationship among composition, structure, and property because of the amorphous nature.

We have recently reported that crystalline composites of Keggin-type POMs with PEGs (POM-PEGs) show moderate proton conductivities under non-humidified and intermediate-temperature conditions<sup>25</sup>. Furthermore, we utilized a Preyssler-type  $[\text{Na}(\text{H}_2\text{O})\text{P}_5\text{W}_{30}\text{O}_{110}]^{14-}$  POM<sup>26</sup>, which is known to show higher acidity as acid salts than Keggin-type POMs, and the POM-PEGs showed proton conductivities of  $10^{-4} \text{ S cm}^{-1}$  under non-humidified and low-temperature conditions<sup>27</sup>. Recently, neutron diffraction and scattering measurements have revealed that a single PEG chain stays as a distorted helix in the channels of POM-PEGs, and that protons are conducted via the PEG chain performing a longitudinal motion along the channel<sup>28</sup>. The longitudinal motion of PEG is localized by the electrostatic interaction with  $\text{Cs}^+$  in the channel<sup>28</sup>. Confinement effects of PEG in nano-channels of metal-organic frameworks (MOFs) have received great attention, and it has been revealed that chemical or physical properties such as transition temperatures of confined PEGs are different from those of the bulk polymer<sup>29</sup>.

Here we show that a Preyssler-type  $[\text{Bi}(\text{H}_2\text{O})\text{P}_5\text{W}_{30}\text{O}_{110}]^{12-}$  POM<sup>30</sup> with a low anion charge facilitates the migration of protons by decreasing the electrostatic interactions between POM and protons. In addition, poly(allylamine) (PAA) is utilized as a polymer because (1) amine groups contribute to increase the number of protonation sites and to extend the hydrogen-bonding network, which results in efficient proton transport and (2) PAA would be positively charged by protonation, and structural stability may improve via electrostatic interaction with POM. Isostructural crystalline composites of Preyssler-type POM with PAAs of different average molecular weights (PAA5000, 3000, and 1600) are synthesized, and the compounds show proton conductivity of  $10^{-2} \text{ S cm}^{-1}$  under mildly-humidified (RH 75%) and low-temperature (368 K) conditions. The compounds with PAA of high average molecular weights (PAA5000 and 3000) show low activation energies in proton conduction (0.16 eV and 0.24 eV) suggesting that protons conduct via rearrangement of the hydrogen-bonding network composed of water molecules and

PAA (i.e., Grotthuss mechanism). On the other hand, the compound with PAA of low average molecular weight (PAA1600) shows a much higher activation energy (0.41 eV) suggesting that the side-chain mobility of PAA contributes to the proton conduction, which is confirmed by NMR spectroscopy. The importance of this work can be summarized as follows: Highly proton conductive but hygroscopic POM and PAA are stabilized via electrostatic interaction in the solid state. While there is a large number of proton-conducting amorphous POM-polymer composites exist, these crystalline composites realize both structure-property relationship and high functionality.

## Results

**Crystal structure.** A composite of POM and PAA5000 was crystallized in an aqueous solution. IR spectroscopy showed that the crystal contained both components (Supplementary Figure 1). The chemical formula of the crystal was determined as  $\text{K}_8\text{H}_4[\text{Bi}(\text{H}_2\text{O})\text{P}_5\text{W}_{30}\text{O}_{110}] \cdot 0.03\text{PAA5000} \cdot 19\text{H}_2\text{O}$  [I] by inductively coupled plasma optical emission spectrometry (ICP-OES), atomic absorption spectrometry (AAS), CHN combustion analysis, and thermogravimetry (TG) (Supplementary Figure 2). Elemental analysis of more than three different lots synthesized with different concentrations of the components in the synthetic solution well agreed with this chemical formula, showing that the chemical formula is uniquely determined and that the amounts of PAA and  $\text{K}^+$  in I is not controllable.

Single-crystal X-ray diffraction (SXRD) analysis showed that the structure of Preyssler-type POM in I agrees with the previous report (Fig. 1a, Supplementary Data 1 and Supplementary Figure 3)<sup>30</sup>: A bismuth atom (Bi(III)) with a coordination water, which are disordered between two positions, exists on the principal axis of the doughnut-shape POM with pseudo- $D_{5h}$  symmetry. The Bi(III) is coordinated by five phosphate oxygens (Bi-O = 2.50–2.73 Å).

Figure 1b–d show the crystal structure of I in the *ab* and *bc* plane, respectively. Eight  $\text{K}^+$  per chemical formula (K1–K12, where K1–K4 and K5–K12 have site occupancies of 1.0 and 0.5, respectively) were located with SXRD analysis as counter cations of POM.  $\text{K}^+$  connects adjacent POMs: K1 has four bonds with POMs (K-O: 2.82–3.01 Å) and links three adjacent POMs. K2 has four bonds with POMs (K-O: 2.88–3.07 Å) and links two adjacent POMs. K3 has four bonds with POMs (K-O: 2.79–3.10 Å) and links two adjacent POMs. K4 has six bonds with POMs (K-O: 2.86–3.08 Å) and links two adjacent POMs. See Supplementary Table 2 and Supplementary Figures 3 and 4 for the details of the local arrangements of POMs with  $\text{K}^+$ . POMs are arranged three-dimensionally in the crystal lattice by the aid of  $\text{K}^+$ , which results in an all-inorganic framework. Void analysis (Fig. 1c, e) shows that three-dimensional channels with a minimum aperture of ca. 4 Å were formed. The void volume of I without the water of crystallization and PAA was 14% ( $995 \text{ \AA}^3$ ,  $Z = 2$ ) of the crystal lattice.

The powder X-ray diffraction (PXRD) pattern (Fig. 2b) well agreed with that calculated from the SXRD data (Fig. 2a), confirming that the crystal structure shown in Fig. 1 represents the whole bulk solid. Besides, the PXRD pattern of  $\text{K}_{12}[\text{Bi}(\text{H}_2\text{O})\text{P}_5\text{W}_{30}\text{O}_{110}] \cdot 26\text{H}_2\text{O}$  (Fig. 2c) was different from that of I, showing that structure change occurs when PAA is accommodated in the crystal lattice. Notably, the use of allylamine monomer instead of PAA resulted in the crystallization of a solid with a different PXRD pattern (Fig. 2d), and this compound was highly soluble in water so that it is not realistic to use it as a solid electrolyte.

**States of PAA in the crystal lattice.** While the position of PAA could not be resolved by SXRD, considering the size of the

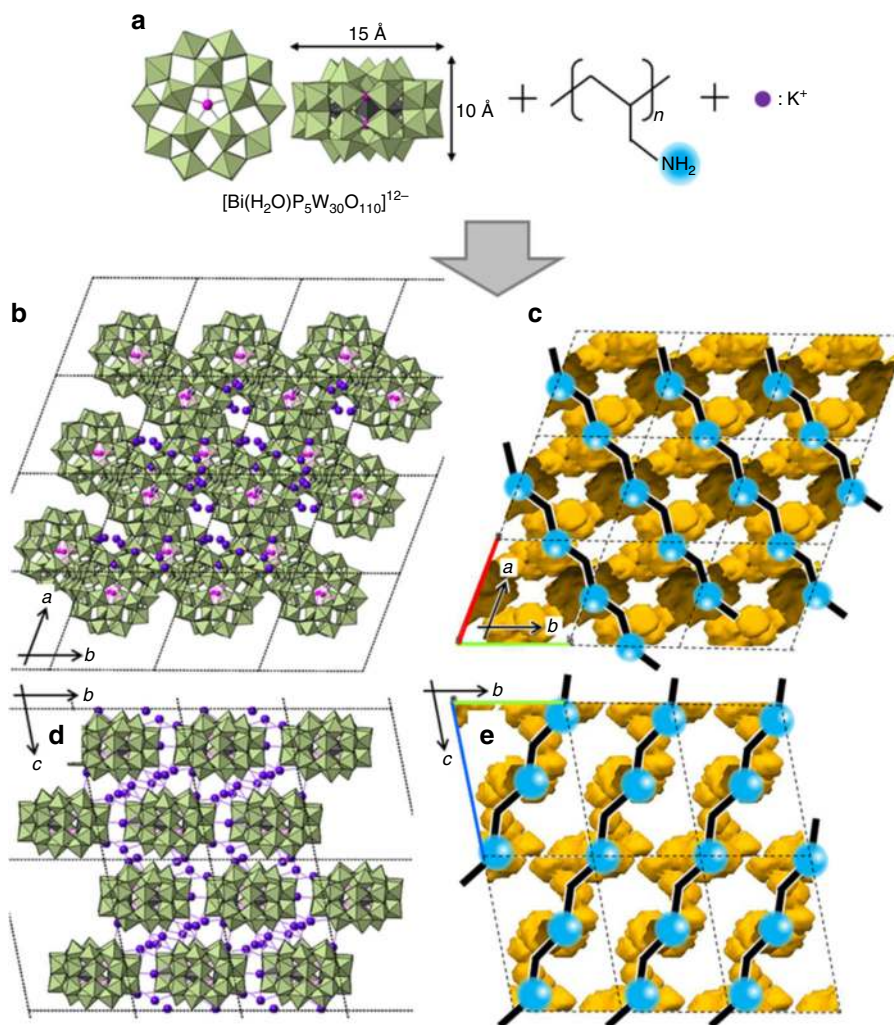


**Fig. 1** Schematic illustration of the synthesis and structures. **a** Molecular structure of Preyssler-type  $[\text{Bi}(\text{H}_2\text{O})\text{P}_5\text{W}_{30}\text{O}_{110}]^{12-}$  POM, and schematic illustration of the synthesis of **I–III**. Crystal structure (**b**) and void analysis (**c**) of **I** in the  $ab$ -plane. Crystal structure (**d**) and void analysis (**e**) of **I** in the  $bc$ -plane. Pink and purple spheres in (**a**), (**b**), and (**d**) show the bismuth and potassium atoms (ions), respectively. Green and gray polyhedra show the  $[\text{WO}_6]$  and  $[\text{PO}_4]$  units, respectively. K–O bonds within bonding distances of 3.2 Å are shown in (**d**). Plausible positions of PAA are shown in (**c**) and (**e**), and molecular and ionic components are omitted for the clarity. Void analysis was carried out by a Mercury structure visualization software (CCDC), and surface of the voids are shown in yellow. Black bold lines and blue spheres show the PAA backbone and amine units, respectively. Red, green, and blue lines in (**c**) and (**e**) indicate the unit cell along the  $a$ ,  $b$ , and  $c$ -axis, respectively. Black broken lines in (**b–e**) are used to display multiple unit cells

channel aperture, PAA probably resides along the  $[111]$  direction with the water of crystallization (see Fig. 1c–e). Packing ratio of PAA in the void was estimated with the void volume ( $995 \text{ \AA}^3$ ,  $Z=2$ ) and number of monomer units of PAA in the unit cell (5.3): Assuming that the volume of PAA monomer unit is ca.  $65 \text{ \AA}^3$ <sup>31</sup>, the packing ratio is 35% ( $=5.3 \times 65/995$ ). Considering that water of crystallization are also contained in the channel, this estimation suggests single-chain accommodation of PAA. In addition, PLATON SQUEEZE<sup>32</sup> has shown that there are 773 electrons per unit cell in the void. Considering that PAA (monomer unit:  $57 \text{ g mol}^{-1}$ ) amounts to 302 electrons ( $=5.3 \times 57$ ) per unit cell, PAA accounts for 39% ( $=302/773$ ) of the electrons in the unit cell, which fairly agrees with the packing ratio. These results suggest that PAA occupies 35–40% of the contents and/or space in the void.

The number of acidic protons ( $\text{H}^+$ ) per chemical formula was estimated as 4 according to the number of potassium ions (8) and anion charge of POM ( $-12$ ). Since the number of acidic protons (4) is larger than the number of monomer units of PAA per chemical formula (2.6), it can be reasonably assumed that the

amine groups of PAA are completely protonated and PAA has become cationic, contributing to stabilize the crystal structure via electrostatic interactions.

In order to confirm the existence of PAA in the crystal lattice, Raman spectra of a single crystal of **I** at different vertical positions (0–30  $\mu\text{m}$  beneath the crystal surface) were measured (Fig. 3)<sup>29</sup>. Bulk poly(allylamine hydrochloride) showed bands at ca. 1450 and  $1350 \text{ cm}^{-1}$ , which can be assigned to C–N stretch and C–H deformation, respectively (Fig. 3b)<sup>33</sup>. Note that POM did not show any bands in this region (Fig. 3a). The Raman spectrum of the surface of a single crystal ( $=$  axial depth of the focal spot is 0  $\mu\text{m}$  from the surface) of **I** showed several high-intensity bands below  $1000 \text{ cm}^{-1}$  and a broad band at  $1300\text{--}1500 \text{ cm}^{-1}$  due to POM and PAA, respectively (Fig. 3c). When the focal spot was set to 10  $\mu\text{m}$  beneath the surface (Fig. 3d), the relative intensity of the broad band at  $1300\text{--}1500 \text{ cm}^{-1}$  increased, and this band was clearly observed when the focal spots were set deeper (Fig. 3e, f). These results confirm the existence of PAA in the crystal lattice.

Differential scanning calorimetry (DSC) measurements were performed to investigate the states of PAA in **I**. The DSC

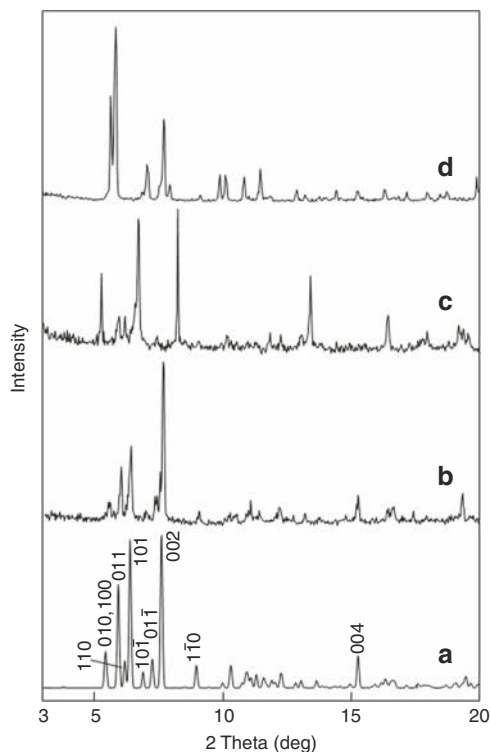


**Fig. 2** PXRD patterns. **a** | (calc) with Miller indices, **b**, **c**  $K_{12}[Bi(H_2O)P_5W_{30}O_{110}] \cdot 26H_2O$ , and **d** the composite of POM with allylamine monomer

curve of the bulk poly(allylamine hydrochloride) showed a small endothermic peak around 380 K, which is in-line with the reported glass transition temperature (Supplementary Figure 5a, b)<sup>34</sup>. On the other hand, no obvious glass transition was observed for **I** (Supplementary Figure 5c). Such a phenomenon was also observed in the case of a single-chain PEG confined in the channel of a POM-PEG composite<sup>28</sup> or a MOF<sup>29</sup>. Generally, temperature dependent glass transitions are molecular cooperative phenomena that a single polymer chain is incapable of displaying.

**Proton conductivity.** Figure 4a (inset) shows the Nyquist plot of the impedance spectrum at 308 K and RH 75%. The bulk proton conductivity was calculated by fitting the Nyquist plot with an electrical equivalent circuit (see Supplementary Methods). The proton conductivity of **I** increased with the temperature (298–368 K, Supplementary Figure 6a) and reached a very high proton conductivity of  $8.5 \times 10^{-3} \text{ S cm}^{-1}$  at 368 K and RH 75%. The activation energy calculated from the Arrhenius plot of the temperature dependent proton conductivities was 0.16 eV (Fig. 4a). It is well known that the activation energy of proton conduction via hydrogen-bonding network rearrangement (Grotthuss mechanism), is about 0.2 eV or less<sup>35</sup>, and proton conduction in Nafions<sup>1</sup> occurs by this mechanism. Notably, the proton conductivity of  $K_{12}[Bi(H_2O)P_5W_{30}O_{110}] \cdot 26H_2O$  was  $3.8 \times 10^{-3} \text{ S cm}^{-1}$  (368 K and RH 75%) and smaller than that of **I**, and the proton conductivity of poly(allylamine hydrochloride) could not be measured because of the hygroscopicity.

**Compounds with PAA of different molecular weights.** Next, compounds with POM and PAA of different average molecular weights (PAA3000 and 1600) were synthesized. The chemical formula of the compounds were determined as  $K_5H_7[Bi(H_2O)P_5W_{30}O_{110}] \cdot 0.11PAA3000 \cdot 16H_2O$  [**II**] and  $K_5H_7[Bi(H_2O)P_5W_{30}O_{110}] \cdot 0.25PAA1600 \cdot 15H_2O$  [**III**]. The PXRD patterns of **II**

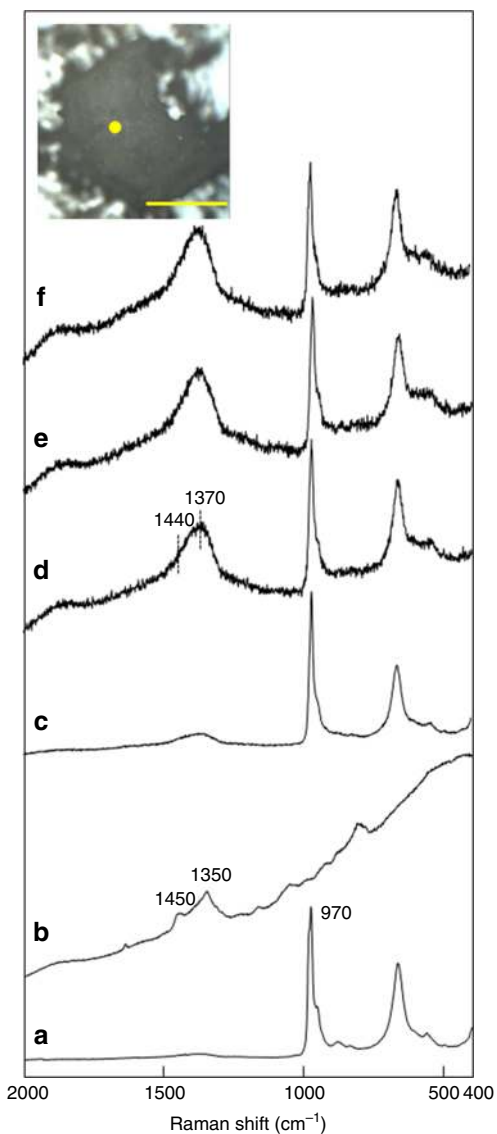


**Fig. 3** Raman spectra and optical microscopic image. Raman spectra of **a**  $K_{12}[Bi(H_2O)P_5W_{30}O_{110}] \cdot 26H_2O$ , **b** poly(allylamine hydrochloride), and **c–f** **I** at different vertical positions at the yellow spot of the optical microscopic image. Yellow bar shows the scale (1 mm). The axial depths of the focal spots are **c** 0  $\mu\text{m}$ , **d** 10  $\mu\text{m}$ , **e** 20  $\mu\text{m}$ , and **f** 30  $\mu\text{m}$  from the crystal surface. The intensities of (**a**) and (**c–f**) were normalized with the band at ca. 970  $\text{cm}^{-1}$ . Note that the increase in relative intensity of the band assignable to PAA (1350–1450  $\text{cm}^{-1}$ ) from (**c**) to (**d–f**) is probably due to the washing of the crystal with water prior to measurement to remove the PAA which adsorbed from the synthetic solution onto the crystal surface

(Supplementary Figure 7b) and **III** (Supplementary Figure 7c) fairly agreed with that of **I** (Fig. 2a and Supplementary Figure 7a), suggesting that the crystal structure is not affected by the average molecular weights of PAA. The amounts of PAA monomer units per chemical formula were estimated as 2.6, 5.8, and 7.0 for **I**, **II**, and **III**, respectively, which increased with the decrease in average molecular weights of PAA. This is probably because accommodation in the crystal lattice becomes more difficult with PAA of longer chains.

Figure 4b, c (inset) show the Nyquist plots of the impedance spectra of **II** and **III**, respectively, at 308 K and RH 75%. The proton conductivities increased with the temperature (298–368 K, Supplementary Figure 6b, c) and reached very high proton

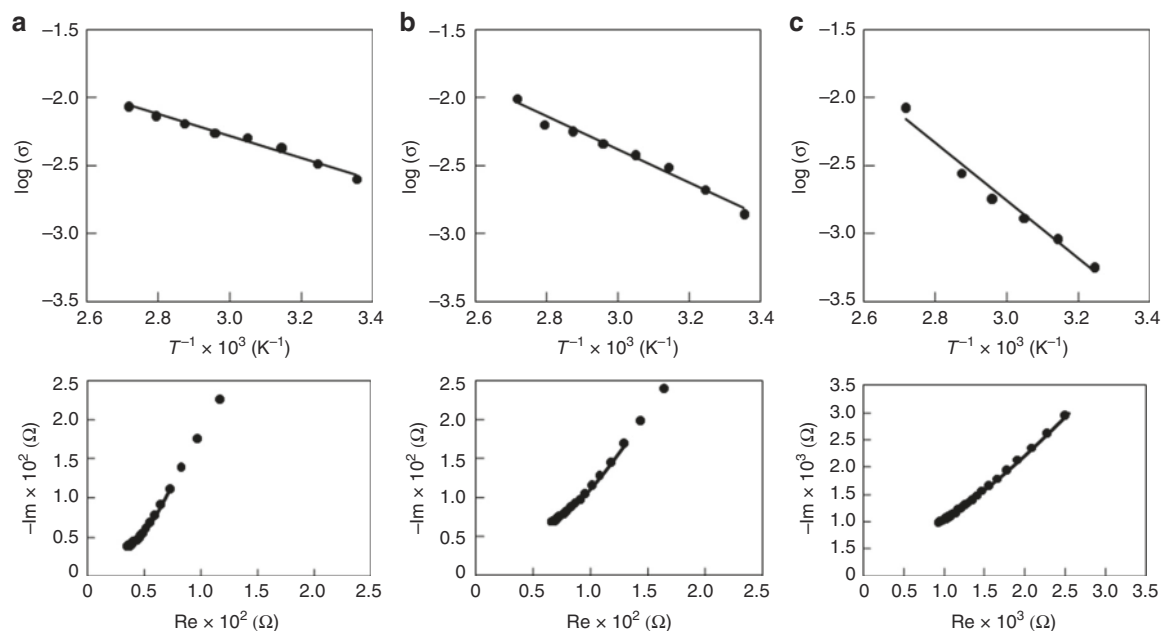


**Fig. 4** Proton conductivities. Arrhenius plots of the proton conductivities of **a** I, **b** II, and **c** III at (298–368 K and RH 75%). Nyquist plot of the impedance spectrum at 308 K (as a representative) is shown under each Arrhenius plot

conductivities of  $9.7 \times 10^{-3}$  and  $8.3 \times 10^{-3}$  S cm<sup>-1</sup> for **II** and **III**, respectively, at 368 K and RH 75%. The proton conductivities of **I–III** at 368 K and RH 75% were within  $8.3\text{--}9.7 \times 10^{-3}$  S cm<sup>-1</sup>, and did not depend much on the average molecular weights of PAA. However, the activation energies estimated from the Arrhenius plots were 0.24 and 0.41 eV for **II** and **III**, respectively (Fig. 4b, c), and showed large differences. According to these results, it can be reasonably assumed that proton conduction in **I** and **II** are based on Grotthuss mechanism, while that of **III** is probably based on vehicle mechanism, or more specifically, segmental motion of the polymer moiety (see below)<sup>25,27,28</sup>. The PXRD patterns before and after the impedance measurement were essentially the same (Supplementary Figure 8), confirming that the crystal structure is stable under this condition.

**States of PAA investigated with NMR spectroscopy.** Solid state magic angle spinning (MAS) NMR spectroscopy was utilized to gain insight into the states of PAA in **I–III**. <sup>1</sup>H-MASNMR spectrum of **I** is shown in Fig. 5a. The signal at 4.3 ppm fairly agrees with the positions of protons of bulk water<sup>36</sup> and PAA backbone (SDBSWeb #4258 allylamine: <http://sdbweb.db.aist.go.jp>, National Institute of Advanced Industrial Science and Technology, Dec. 19th, 2018). The signal at 7.3 ppm agrees with the position of methylene protons of the PAA side-chain (SDBSWeb #4258 allylamine: <http://sdbweb.db.aist.go.jp>, National Institute of Advanced Industrial Science and Technology, Dec. 19th, 2018). Compounds **II** and **III** gave <sup>1</sup>H-MASNMR spectra similar to that of **I** (Supplementary Figure 9). Then, in order to compare the local mobility of PAA, variable contact time <sup>13</sup>C cross-polarization MAS (<sup>13</sup>C-CPMAS) NMR spectroscopy was used. Time constants for magnetization buildup ( $T_{\text{CH}}$ ) and subsequent decay ( $T_{1\rho(\text{H})}$ ) can be obtained according to the following equation,

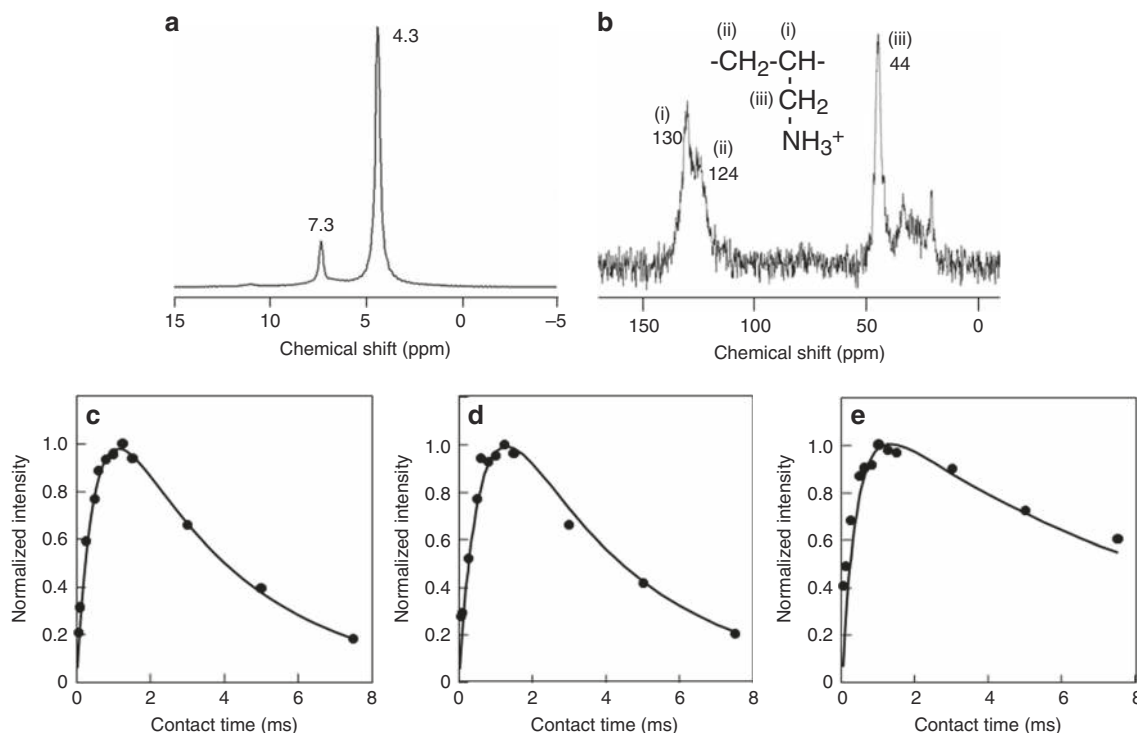
$$I(t) = I_0(1 - T_{\text{CH}}/T_{1\rho(\text{H})})^{-1} \{ \exp(-t/T_{1\rho(\text{H})}) - \exp(-t/T_{\text{CH}}) \} \quad (1)$$

where  $I(t)$  shows the intensity of the signal at contact time  $t$ , and

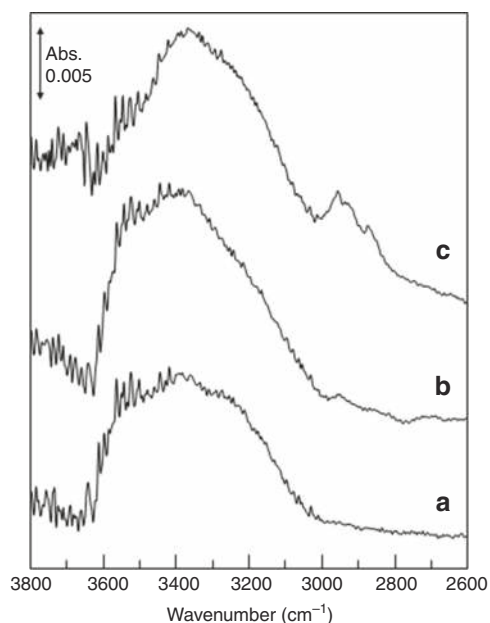
$I_0$  shows the theoretical maximum intensity<sup>37</sup>.  $T_{1\rho(\text{H})}$  can be used to semi-quantify the local mobility, which is longer if the polymer chain is more mobile<sup>38</sup>.

Figure 5b shows the solid-state <sup>13</sup>C-CPMASNMR spectrum of **I**, and each signal can be reasonably assigned to each carbon moiety of PAA (SDBSWeb #4258 allylamine: <http://sdbweb.db.aist.go.jp>, National Institute of Advanced Industrial Science and Technology, Dec. 19th, 2018). Compounds **II** and **III** gave <sup>13</sup>C-CPMASNMR spectra similar to that of **I**. Figure 5c–e show the changes in intensities of the methylene side-chain carbon signal of PAA in **I–III**, respectively, with variations of contact time (see Supplementary Figure 10 for the raw data). The intensities of the signals increased, reached maximum, and then decreased. The magnetization decay of **III** was much slower than those of **I** and **II**, showing that  $T_{1\rho(\text{H})}$  is longer and thus mobility of the methylene side-chain carbon of PAA is higher.  $T_{1\rho(\text{H})}$  values were estimated as 3.5, 3.6, and 9.5 ms for **I**, **II**, and **III**, respectively, with eq. (1). This result suggests that side-chain mobility of **III** with the lowest average molecular weight of PAA (i.e., PAA1600) is faster than those of higher molecular weights. It has been reported that activation energies for the side-chain mobility of polymers in the solid state are at least 0.2 eV and sometimes larger than 1 eV depending on the backbone and side-chain structures<sup>39,40</sup>. Considering that the protonated amine group resides on the side-chain of PAA and the trend in activation energies of proton conduction (**I**: 0.16 eV  $\approx$  **II**: 0.24 eV < **III**: 0.41 eV), it can be concluded that the side-chain mobility of PAA is crucial to the proton conduction in **III**. Notably, the difference among the  $T_{1\rho(\text{H})}$  values of carbon atoms of PAA backbone were not so large, probably because the longitudinal motion of PAA is localized by the electrostatic interactions with K<sup>+</sup> and POM in the channel, as in the case of POM-PEGs<sup>28</sup>.

**States of water molecules investigated with IR spectroscopy.** Finally, the states of water molecules in **I–III** were investigated with the  $\nu(\text{OH})$  bands of the in situ IR spectra under water vapor at rt (Fig. 6, see Supplementary Figures 11–13 for the details). Note that the proton conductivities were in the order of  $5.6 \times$



**Fig. 5** Solid state MASNMR spectroscopy. **a**  $^1\text{H}$ -MASNMR (MAS = 10 KHz) and **b**  $^{13}\text{C}$ -CPMASNMR (MAS = 5 kHz, contact time = 2 ms) of **I** at rt. Changes in the intensities of the side-chain methylene carbon signal (44 ppm) of **c I**, **d II**, and **e III** with variation of contact time. In **(b)**, (i) and (ii) show the tertiary and secondary carbons of PAA backbone, respectively, and (iii) shows the methylene carbon of PAA side-chain. Experimental and calculated (eq. 1) data are shown by the circles and solid lines, respectively. Intensities are normalized by the largest signal in each plot. Note that  $T_{1\rho}(\text{H})$  of poly (allylamine hydrochloride) ( $m = 120,000$ , Alfa Aesar) measured and calculated under the same experimental conditions was 3.4 ms



**Fig. 6** IR spectra of **I–III** under a water vapor pressure of  $1 \times 10^3$  Pa at room temperature. **a I**, **b II**, and **c III**. Double-headed arrow along the y-axis shows the scale of absorbance (0.005)

$10^{-4} \text{ S cm}^{-1}$  (**III**)  $< 2.1 \times 10^{-3} \text{ S cm}^{-1}$  (**II**)  $\approx 3.3 \times 10^{-3} \text{ S cm}^{-1}$  (**I**) around rt (308 K) and RH 75%. Upon the introduction of water vapor, a broad band appeared around  $3600\text{--}3000 \text{ cm}^{-1}$  for all compounds. The band was rather sharp and a maximum was observed around  $3400 \text{ cm}^{-1}$  for **III**. On the other hand, the band extended toward the higher frequency (wavenumber)

( $3500\text{--}3600 \text{ cm}^{-1}$ ) for **I** and **II**, and also toward the lower frequency ( $3200 \text{ cm}^{-1}$ ) for **I**. Previous reports by us and other groups have shown that the bands at high ( $3500\text{--}3600 \text{ cm}^{-1}$ ) and low ( $3200\text{--}3400 \text{ cm}^{-1}$ ) frequencies can be attributed to unperturbed (free) water molecules at the outside of a water cluster and to perturbed hydrogen-bonded water molecules inside the cluster, respectively<sup>41,42</sup>. Therefore, it can be reasonably stated that **I** possesses an extensive hydrogen-bonding network of water molecules and PAA, which agrees with the relatively large number of the water of crystallization (19 (**I**)  $>$  16 (**II**), 15 (**III**)), and free water molecules (protons) at the periphery of the hydrogen-bonding network.

## Discussion

According to these results, the relationship between proton conductivity and states of water molecules and PAA in the compounds can be interpreted as follows. The mobile water molecules (protons) as well as the extensive hydrogen-bonding network probably contribute to the efficient proton conduction and low activation energy of **I** (0.16 eV). Both the relative intensities of the IR bands at high frequencies and proton conductivities (308 K and RH 75%) were in the order of **I**  $\approx$  **II**  $>$  **III**, and activation energies of proton conduction was in the order of **I** (0.16 eV)  $\approx$  **II** (0.24 eV)  $<$  **III** (0.41 eV). Therefore, it can be concluded that mobile water molecules (protons) largely contribute to the efficient proton conduction and low activation energies of **I** and **II**, while water molecules are rather fixed and the side-chain mobility of PAA is crucial to the proton conduction in **III**.

In summary, we have shown that the low durability of POM and PAA due to hygroscopicity was circumvented by the electrostatic interaction between the POM and protonated amine moieties in the solid state, and proton conductivities of  $10^{-2} \text{ S cm}^{-1}$  were

achieved under mild-humidity (RH 75%) and low-temperature (368 K) conditions. Spectroscopic studies have revealed that the side-chain mobility of PAA and hydrogen-bonding network rearrangement contribute to the proton conduction in compounds with PAA of low and high average molecular weights, respectively. We will report the states and dynamics of protons, water, and polymers in the near future.

## Methods

**Materials.** Potassium salt of Preyssler-type POM ( $K_{12}[Bi(H_2O)P_5W_{30}O_{110}] \cdot 26H_2O$ ) was synthesized according to a previously reported method<sup>30</sup>. Forty percent aqueous poly(allylamine hydrochloride) solution ( $m = 5000, 3000, \text{ or } 1600$ ) was provided from Nittobo Medical Co., Ltd. Allylamine hydrochloride and poly(allylamine hydrochloride) ( $m = 120,000$ ) were purchased from Kanto Chemical Co. and Alfa Aesar, respectively, and used as received.

**Synthesis.** Compounds I–III were synthesized as follows: 1.0 g of  $K_{12}[Bi(H_2O)P_5W_{30}O_{110}] \cdot 26H_2O$  (0.12 mmol) was dissolved in 20 mL of  $H_2O$  (solution A). Six milliliters of  $H_2O$  was added to 3.0 g of 40% aqueous poly(allylamine hydrochloride) solution ( $m = 5000, 3000, \text{ or } 1600$ ) (solution B). Solution B was added to solution A, and the solution was left for 1 week at 278 K. Colorless crystals of I–III were obtained in ca. 70% yield. As for the synthesis of the compound with allylamine (i.e., monomer), equal amount of monomer in mole was used instead of PAA. Elemental analysis (calcd) for  $K_8H_4[Bi(H_2O)P_5W_{30}O_{110}] \cdot 0.03PAA5000 \cdot 19H_2O$  [I]: C 1.23 (1.25), H 0.59 (0.77), N 0.63 (0.48), K 3.6 (3.7), Bi 2.6 (2.5), P 2.1 (1.8), W 63 (65). Elemental analysis (calcd) for  $K_5H_7[Bi(H_2O)P_5W_{30}O_{110}] \cdot 0.11PAA3000 \cdot 16H_2O$  [II]: C 2.38 (2.50), H 0.47 (0.95), N 1.19 (0.97), K 2.3 (2.3), Bi 2.1 (2.4), P 2.1 (1.8), W 62 (64). Elemental analysis (calcd) for  $K_5H_7[Bi(H_2O)P_5W_{30}O_{110}] \cdot 0.25PAA1600 \cdot 15H_2O$  [III]: C 2.98 (2.87), H 0.74 (1.04), N 1.67 (1.11), K 2.3 (2.3), Bi 2.3 (2.4), P 1.8 (1.8), W 61 (63). Elemental analysis of more than 3 different lots for each compound well agreed with these formulae.

**SXRD analysis.** X-ray diffraction data of I was collected at 93 K with a CCD 2-D detector by using Rigaku Saturn diffractometer with graphite monochromated Mo K $\alpha$  radiation. Structures were solved by direct methods (SHELX97), expanded using Fourier techniques, and refined by full-matrix least squares against  $F^2$  with the SHELXL-2014 package. Tungsten atoms and part of the potassium atoms were refined anisotropically. Phosphorus, oxygen, bismuth, and other potassium atoms were refined isotropically. Hydrogen atoms, PAA, and water of crystallization were not included in the model. Bismuth atom was disordered between two positions with site occupancies of 0.8 and 0.2. Such disordering of central metal ions ( $Na^+, K^+, Tb^{3+}, Eu^{3+}$ ) with a water molecule has been observed for several Preyssler-type POMs<sup>43–45</sup>. Void analysis was carried out by Mercury structure visualization software (CCDC) with a probe radius of 2.0 Å and approximate grid spacing of 0.7 Å and PLATON SQUEEZE<sup>32</sup>. Crystal data for I: triclinic P-1 (No. 2),  $a = 17.80(2)$  Å,  $b = 18.018(19)$  Å,  $c = 24.68(3)$  Å,  $\alpha = 75.28$  (8),  $\beta = 78.97(8)$ ,  $\gamma = 67.75(6)$ ,  $V = 7046(14)$ ,  $Z = 2$ ,  $R_1 = 0.1100$ ,  $wR_2 = 0.2880$ , GOF = 1.122.

**Measurements.** Combustion analysis (Elementar, vario MICRO cube) was used for the quantitative analysis of C, H, and N. ICP-OES (Agilent Technologies, ICP-OES720) was used for the quantitative analysis of Bi, P and W. AAS (Hitachi, ZA3000) was used for the quantitative analysis of K. Prior to the ICP-OES and AAS analysis, ca. 10 mg of the solid (accurately weighed) was dispersed in 10 mL of  $H_2O$  with NaOH (0.2 g) to dissolve the solid completely, conc.  $HNO_3$  (0.3 mL) was added, and the solution was diluted up to exactly 100 mL. PXRD patterns were measured with a New advance D8 X-ray diffractometer (Bruker) by using Cu K $\alpha$  radiation ( $\lambda = 1.54056$  Å, 40 kV–40 mA) at  $2\theta = 3 - 20^\circ$  and  $1.8^\circ \text{ min}^{-1}$ . Solid-state MASNMR spectra (MAS rate = 5 and 10 kHz for  $^{13}C$  and  $^1H$ , respectively) were recorded with an AVANCE 400WB spectrometer (Bruker), and the resonance frequencies were 100.6 and 400.2 MHz for  $^{13}C$  and  $^1H$ , respectively. Adamantane ( $^1H$  1.91 ppm,  $^{13}C$  28.8 and 38.3 ppm) was used as an external standard for the calibration of chemical shifts. Single-pulse excitation ( $^1H$ ) or cross-polarization (CP) with contact times of 0.05–7.5 ms ( $^{13}C$ ) were used for the NMR measurements. Micro-Raman measurements were performed using a JASCO NRS-4500 spectrometer with an excitation wavelength of 785 nm. The beam was focused onto the sample using an optical microscope ( $\times 100$  magnification), which allowed us to focus the laser beam with a 1  $\mu\text{m}$  lateral resolution and an axial depth resolution of 1.5  $\mu\text{m}$ . Alternating current (AC) impedance measurements: About 0.3 g of each compound was compressed at 150 kgf  $\text{cm}^{-2}$  into pellets of 10 mm in diameter and ca. 1.0 mm in thickness. The pellets were cut into fourths, and one-fourth of the pellet was used for the AC impedance measurement. AC impedance measurements were carried out in a temperature and humidity chamber with a BioLogic VMP3 multichannel potentiostat/galvanostat (Science Instruments) over the frequency range of 2 Hz to 2 MHz and AC amplitude of 500 mV. Gold electrodes with copper wire were attached on both faces of the pellets. Bulk conductivities were estimated by a semicircle fitting of Nyquist plots. An electrical equivalent circuit, which

consists of a series of inductance ( $H$ , representing the effect of the external circuit) and three blocks of a resistance ( $R$ ) and constant phase element (CPE, used for imperfect capacitors) in parallel, standing for bulk, grain boundary, and electrode interface, was used to fit the impedance spectra (see Supplementary Methods for the details). In situ IR spectra under water vapor were measured as follows: Each powder sample was deposited on a  $CaF_2$  plate (20 mm diameter), which was placed inclined at the center of an IR cell, and treated in vacuo at 298 K for 0.5 h. IR spectra were obtained at a resolution of  $4 \text{ cm}^{-1}$  by averaging 64 scans using a Jasco 6100 FT-IR spectrometer equipped with an MCT detector. The IR spectra of the sample in vacuum were recorded as background spectra. IR spectra of adsorbed water were measured by increasing the water vapor pressure from 5 to  $1 \times 10^3$  Pa at rt, and background-subtracted IR spectra showing adsorbed water are presented throughout this paper.

## Data availability

The X-ray crystallographic coordinates for the structure of compound I is available as Supplementary Tables 1 and 2. The data has also been deposited at the Cambridge Crystallographic Data Centre (CCDC) under deposition number 1856730. The data can be obtained free of charge from the CCDC via [http://www.ccdc.cam.ac.uk/data\\_request/cif](http://www.ccdc.cam.ac.uk/data_request/cif). The other data that support the findings of this study are available from the corresponding author upon reasonable request.

Received: 26 September 2018 Accepted: 7 January 2019

Published online: 25 January 2019

## References

1. Mauritz, K. A. & Moore, R. B. State of understanding of Nafion. *Chem. Rev.* **104**, 4535–4546 (2004).
2. Quartarone, E., Mustarelli, P. & Magistris, A. PEO-based composite polymer electrolytes. *Solid State Ion.* **110**, 1–14 (1998).
3. Gadjourova, Z., Andreev, Y. G., Tunstall, D. P. & Bruce, P. G. Ionic conductivity in crystalline polymer electrolytes. *Nature* **412**, 520–523 (2001).
4. Li, Y. et al. Enhancing sodium-ion battery performance with interlayer-expanded  $MoS_2$ -PEO nanocomposites. *Nano Energy* **15**, 453–461 (2015).
5. Meng, X., Wang, H. -N., Song, S. -Y. & Zhang, H. -J. Proton-conducting crystalline porous materials. *Chem. Soc. Rev.* **46**, 464–480 (2017).
6. Pope, M. T. & Müller, A. Polyoxometalate chemistry: an old field with new dimensions in several disciplines. *Angew. Chem. Int. Ed.* **30**, 34–48 (1991).
7. Hill, C. L. Stable, self-assembling, equilibrating catalysts for green chemistry. *Angew. Chem. Int. Ed.* **43**, 402–404 (2004).
8. Izarova, N. V., Pope, M. T. & Kortz, U. Noble metals in polyoxometalates. *Angew. Chem. Int. Ed.* **51**, 9492–9510 (2012).
9. Busche, C. et al. Design and fabrication of memory devices based on nanoscale polyoxometalate clusters. *Nature* **515**, 545–549 (2014).
10. Zhang, Z. et al. Ultrathin inorganic molecular nanowire based on polyoxometalates. *Nat. Commun.* **6**, 7731 (2015).
11. Seino, S., Kawahara, R., Ogasawara, Y., Mizuno, N. & Uchida, S. Reduction-induced selective uptake of cesium ions by an ionic crystal based on silicododecamolybdate. *Angew. Chem. Int. Ed.* **55**, 3987–3991 (2016).
12. Ma, H. et al. Cationic covalent organic frameworks: a simple platform of anionic exchange for porosity tuning and proton conduction. *J. Am. Chem. Soc.* **138**, 5897–5903 (2016).
13. Ye, Y. et al. Straightforward loading of imidazole molecules into metal-organic framework for high proton conduction. *J. Am. Chem. Soc.* **139**, 15604–15607 (2017).
14. Cao, X. -L. et al. A well-established POM-based single-crystal proton-conducting model incorporating multiple weak interactions. *Chem. Eur. J.* **24**, 2365–2369 (2018).
15. Liu, J. -C. et al. Aggregation of giant cerium-bismuth tungstate clusters into a 3D porous framework with high proton conductivity. *Angew. Chem. Int. Ed.* **57**, 8416–8420 (2018).
16. Yang, P., Alsufyani, M., Emwas, A. -H., Chen, C. & Khashab, N. M. Lewis acid guests in a  $\{P_8W_{48}\}$  archetypal polyoxotungstate host: enhanced proton conductivity via metal-oxocluster within cluster assemblies. *Angew. Chem. Int. Ed.* **57**, 13046–13051 (2018).
17. Nakamura, O., Kodama, T., Ogino, I. & Miyake, Y. High-conductivity solid proton conductors: dodecamolybdophosphoric acid and dodecatungstophosphoric acid crystals. *Chem. Lett.* **8**, 17–18 (1979).
18. Xie, Z., Wu, H., Wu, Q. & Ai, L. Synthesis and performance of solid proton conductor molybdovanadosilicic acid. *RSC Adv.* **8**, 13984–13988 (2018).
19. Xie, Z., Wu, Q., He, F. & Ai, L. Synthesis and conductive performance of quaternary heteropoly acid  $H_5SiW_9Mo_2VO_{40} \cdot 13H_2O$ . *Funct. Mater. Lett.* **11**, 1850065 (2018).

20. Tong, X. et al. Preparation and electrochemical performance of tungstovanadophosphoric heteropoly acid and its hybrid materials. *J. Phys. Chem. C* **117**, 3258–3263 (2013).
21. Zhang, L. et al. Inorganic-macroion-induced formation of bicontinuous block copolymer nanocomposites with enhanced conductivity and modulus. *Angew. Chem. Int. Ed.* **56**, 9013–9017 (2017).
22. Lai, X. et al. Controllable proton-conducting pathways via situating polyoxometalates in targeting pores of a metal-organic framework. *J. Mater. Chem. A* **5**, 9611–9617 (2017).
23. Miao, J. et al. Proton conducting polyoxometalate/polypyrrole films and their humidity sensing performances. *ACS Appl. Nano Mater.* **1**, 564–571 (2018).
24. Wu, H., Wu, X., Wu, Q. & Yan, W. High performance proton-conducting composite based on vanadium-substituted Dawson-type heteropoly acid for proton exchange membranes. *Compos. Sci. Technol.* **162**, 1–6 (2018).
25. Tsuboi, M., Hibino, M., Mizuno, N. & Uchida, S. Crystalline polyoxometalate (POM)–polyethylene glycol (PEG) composites aimed as non-humidified intermediate-temperature proton conductors. *J. Solid State Chem.* **234**, 9–14 (2016).
26. Sadakane, M., Ichi, Y., Ide, Y. & Sano, T. Thermal stability and acid strength of Preyssler-type phosphotungstic acid,  $H_{14}[P_5W_{30}O_{110}Na]$  and its catalytic activity for hydroxylation of alkyl acetate. *Z. Anorg. Allg. Chem.* **637**, 2120–2124 (2011).
27. Niinomi, K., Miyazawa, S., Hibino, M., Mizuno, N. & Uchida, S. High proton conduction in crystalline composites based on Preyssler-type polyoxometalates and polymers under non-humidified or humidified conditions. *Inorg. Chem.* **56**, 15187–15193 (2017).
28. Wu, H. et al. Spatial-temporal characteristics of confined PEG motion determine proton conduction of polyoxometalate-PEG hybrid nanocomposites. *J. Phys. Chem. Lett.* **9**, 5572–5777 (2018).
29. Uemura, T. et al. Unveiling thermal transitions of polymers in subnanometre pores. *Nat. Commun.* **1**, 83 (2010).
30. Hayashi, A. et al. Cation effect on formation of Preyssler-type 30-tungsto-5-phosphate: enhanced yield of Na-encapsulated derivative and direct synthesis of Ca- and Bi-encapsulated derivatives. *Z. Anorg. Allg. Chem.* **641**, 2670–2676 (2015).
31. Zhao, Y. H., Abraham, M. H. & Zissimos, A. M. Fast calculation of van der Waals volume as a sum of atomic and bond contributions and its application to drug compounds. *J. Org. Chem.* **68**, 7368–7373 (2003).
32. Spek, A. L. PLATON SQUEEZE: a tool for the calculation of the disordered solvent contribution to the calculated structure factors. *Acta Cryst. C* **71**, 9–18 (2015).
33. Zucolotto, V. et al. Unusual interactions binding iron tetrasulfonated phthalocyanine and poly(allylamine hydrochloride) in layer-by-layer films. *J. Phys. Chem. B* **107**, 3733–3737 (2003).
34. Shao, L. & Lutkenhaus, J. L. Thermochemical properties of free-standing electrostatic layer-by-layer assemblies containing poly(allylamine hydrochloride) and poly(acrylic acid). *Soft Matter* **6**, 3363–3369 (2010).
35. Kreuer, K. D. Proton conductivity: materials and applications. *Chem. Mater.* **8**, 610–641 (1996).
36. Gottlieb, H. E., Kotlyar, V. & Nudelman, A. NMR chemical shifts of common laboratory solvents as trace impurities. *J. Org. Chem.* **62**, 7512–7515 (1997).
37. Fyfe, C. A., Diaz, A. C., Grondy, H., Lewis, A. R. & Förster, H. Solid state NMR method for the determination of 3D zeolite framework/sorbate structures:  $^1H/^{29}Si$  CP MAS NMR study of the high-loaded form of *p*-xylene in ZSM-5 and determination of the unknown structure of the low-loaded form. *J. Am. Chem. Soc.* **127**, 7543–7558 (2005).
38. Naik, V. V. & Vasudevan, S. Effect of alkyl chain arrangement on conformation and dynamics in a surfactant intercalated layered double hydroxide: spectroscopic measurements and MD simulations. *J. Phys. Chem. C* **115**, 8221–8232 (2011).
39. Mccreight, K. W. et al. Phase structures and transition behaviors in polymers containing rigid rodlike backbones with flexible side chains. V. Methylene side-chain effects on structure and molecular motion in a series of polyimides. *J. Polym. Sci. B Polym. Phys.* **37**, 1633–1646 (1999).
40. Ryu, S. -Y., Chung, J. W. & Kwak, S. -Y. Probing the role of side-chain interconnecting groups in the structural hydrophobicity of comblike fluorinated polystyrene by solid state NMR spectroscopy. *Langmuir* **31**, 9473–9482 (2015).
41. Jentys, A., Warecka, G., Derewinski, M. & Lercher, J. A. Adsorption of water on ZSM 5 zeolites. *J. Phys. Chem.* **93**, 4837–4843 (1989).
42. Uchida, S. et al. Proton conduction in alkali metal ion-exchanged porous ionic crystals. *Phys. Chem. Chem. Phys.* **19**, 29077–29083 (2017).
43. Lu, Y., Li, Y., Wang, E., Xu, X. & Ma, Y. A new family of polyoxometalate compounds built up of Preyssler anions and trivalent lanthanide cations. *Inorg. Chim. Acta* **360**, 2063–2070 (2007).
44. Hu, T.-P. et al. Four hybrid materials based on Preyssler  $P_5W_{30}$  polyoxometalate and first-row transition-metal complex. *Inorg. Chem.* **54**, 7415–7423 (2015).
45. Kato, C. et al. Giant Hysteretic Single-Molecule Electric Polarisation Switching above Room Temperature. *Angew. Chem. Int. Ed.* **57**, 13429–13432 (2018).

### Acknowledgements

This work was supported by JST-PRESTO (JPMJPR1312) and grant-in-aids for scientific research JP16K05742 and JP17H05356 (Coordination Asymmetry) from MEXT of Japan. Prof. M. Matsuo and Dr. K. Shozugawa (Univ. of Tokyo) are acknowledged for providing access to the ICP instrument.

### Author contributions

T.I., S.M., and S.U. designed and carried out the experiments, and wrote the manuscript. R.O. and J.N.K. designed and performed the in situ IR measurements. K.H., T.K., and T.U. designed and performed the DSC and Raman measurements.


### Additional information

Supplementary information accompanies this paper at <https://doi.org/10.1038/s42004-019-0111-x>.

**Competing interests:** The authors declare no competing interests.

**Reprints and permission** information is available online at <http://npg.nature.com/reprintsandpermissions/>

**Publisher's note:** Springer Nature remains neutral with regard to jurisdictional claims in published maps and institutional affiliations.

 **Open Access** This article is licensed under a Creative Commons Attribution 4.0 International License, which permits use, sharing, adaptation, distribution and reproduction in any medium or format, as long as you give appropriate credit to the original author(s) and the source, provide a link to the Creative Commons license, and indicate if changes were made. The images or other third party material in this article are included in the article's Creative Commons license, unless indicated otherwise in a credit line to the material. If material is not included in the article's Creative Commons license and your intended use is not permitted by statutory regulation or exceeds the permitted use, you will need to obtain permission directly from the copyright holder. To view a copy of this license, visit <http://creativecommons.org/licenses/by/4.0/>.

© The Author(s) 2019